This file is the final accepted version of the manuscript, published in
https://doi.org/10.1061/JSENDH.STENG-12684

# WIND-TUNNEL TESTING OF LOW- AND MID-RISE BUILDINGS UNDER HETEROGENEOUS UPWIND TERRAINS

Nasrollah Alinejad[a], Sejin Kim[b], Sungmoon Jung[c*]

[a] Department of Civil and Environmental Engineering, FAMU-FSU College of Engineering, Tallahassee, FL 32310, USA (Email: nalinejad@fsu.edu)

[b] Department of Civil and Environmental Engineering, University of Michigan, Ann Arbor, MI 48109, USA (Email: sejinki@umich.edu)

[c] Department of Civil and Environmental Engineering, FAMU-FSU College of Engineering, Tallahassee, FL 32310, USA ([*]Corresponding author's Email: sjung@eng.famu.fsu.edu)

## Abstract

An extensive series of wind tunnel experiments were conducted in the Boundary Layer Wind Tunnel (BLWT) Experimental Facility (EF) at the University of Florida (UF) to investigate the effect of heterogenous terrain on wind flow and pressure distributions on building surfaces. Many studies have already been performed on the effect of upwind terrain on wind characteristics and wind loads on buildings. Previous tests in wind tunnels were mainly designed for uniform upwind terrain or simple 2D roughness changes (e.g., smooth-to-rough change or vice versa). Using the wind tunnel facility at the UF, we were able to perform an extensive series of tests on heterogeneous upwind terrains. The first part of the testing was focused on wind characteristics by measuring the three components of wind velocity when wind flow passed over different complex upwind terrains. The second part of the testing was intended to obtain the aerodynamic loads of wind over complex terrains on low-rise and mid-rise building models. The data and metadata are

publicly available on the DesignSafe-CI repository under the DOI of 10.17603/Ds2-6hg9-R131. Researchers and practicing engineers can use the collected data to understand the effect of heterogeneous upwind terrain better.

**Keywords:** Wind tunnel, Heterogeneous terrain, Low-rise building model, Mid-rise building model

## 1. Introduction

Many of the previous wind tunnel tests for low- and mid-rise buildings were carried out under simplified upwind terrain conditions due to the difficulties of the simulating generic heterogeneous terrain setup in the wind tunnel. Uniform terrain, namely open or suburban areas, was commonly adopted for the terrain setup (Fernández-Cabán & Masters, 2020; Sabareesh et al., 2013; Zisis & Stathopoulos, 2010; Wang & Stathopoulos, 2006). Some researchers tried to simulate nonuniform upwind terrain, however, the effort was limited to 2D roughness changes in which the upwind terrain had multiple step changes parallel to the wind flow while remaining uniform in the perpendicular direction of the flow (Deaves, 1981; Wang and Stathopoulos, 2007). Considering the significant effect of the upwind terrain on pressure distributions on buildings (Chen et al., 2018; Lim et al., 2014), these simplified setups have inherent limitations to simulate realistic wind and pressure distribution at the building position, emphasizing the necessity of exploring the effect of various heterogeneous terrain in the wind tunnel. Balderrama et al. (2012) stated that the field records show positive non-Gaussian wind speed distribution, which increases the possibility of extreme values. However, the possibility of observing a non-Gaussian trend is low under uniform simulation of upwind terrain in the wind tunnel. Relying on uniform upwind terrain will have a significant inaccuracy in peak factor analysis. Moreover, the uniform simulation of upwind terrain

will produce an equilibrium state in the upcoming flow, while in the real world, the equilibrium state does not hold when the upwind terrain is complex.

An extensive series of wind tunnel tests were performed to investigate the effect of generic heterogeneous upwind terrain on wind loads on buildings. In the first phase, wind speed distributions at the end of the upwind terrain patch were measured for 180 different heterogeneous upwind terrains. In the second phase, two building models, low-rise and mid-rise models, were placed in front of the roughness elements and the pressure on the models was measured using a scanivalve pressure scanning system. The following sections briefly explain the wind tunnel facilities, building models used for testing and upwind terrain configurations. In sections 5 and 6, the data collection and validation for wind speed measurement and wind pressure measurement are discussed. Section 7 shows how the data and metadata files are organized and can be accessed through the DesignSafe-CI repository.

## 2. Testing Facilities and Instruments

### 2.1. Wind-Tunnel Specification

The Boundary Layer Wind Tunnel (BLWT) Experimental Facility (EF) at the University of Florida (UF) was used in this study. The schematic profile of BLWT is shown in Figure 1. The BLWT upwind fetch, called Terraformer, consisted of 18 × 62 cubic roughness elements. Each roughness element had a plan area of 5 cm × 10 cm. The height of roughness elements varied from 0 to 16 cm with the aid of an actuator beneath every one of them. The spacing between roughness elements was 30 cm, and they were arranged in a staggered fashion. The dimension of upwind fetch was 18.6 m × 6.1 m, which was in front of a turntable where the building model will be located. The

multi-fan Flow Field Modulator (FFM) was mounted in front of the fan bank to control the wind pattern in the BLWT.

### 2.2. Instrumentation

In this project, two categories of testing, wind speed measurement and wind pressure measurement, were conducted. Three Turbulent Flow Cobra Probes measure the longitudinal, transverse and vertical components of wind velocity. For the wind speed profile, the probes were located at the end of Terraformer (x = +29.5 m). For most profile testing, the probes were located at y = 0.00 m. However, for 10 cases, the gantry system which holds the probes was moved laterally to y = ± 0.3 m and ± 0.6 m, because unlike uniform simulation of upwind terrain, the wind characteristic of nonuniform terrain would not be the same in different lateral locations. The vertical location of the probes varies from 0.01 m up to 1.505 m above the ground level. The sampling rate was 1250 Hz for this part of the testing.

For the pressure measurement, a 625 Hz Scannivalve ZOC33 pressure scanning system located under the turntable center as well as the Cobre Probes instrumentation, were used. Two building models- which will be described in section 3- were placed at the center of the turntable at x = 31.5 m. To avoid any disturbance in the flow, the probes were moved to x = 30 m, y = 0.5 m and z = eave height of the models for obtaining the reference velocity.

## 3. Building Models

### 3.1. Low-rise Model

The low-rise model was created after Texas Tech University (TTU) building (Cheung et al., 1997; Levitan & Mehta, 1992). The model scale was 1:50 for wind-tunnel testing. The justification for model scale can be found in Kopp et al. (2005). The full-scale dimensions of the TTU building are 13.7 m (length) by 9.1 m (width) and 4 m (height), which leads to 27.45 cm by 18.25 cm by 8 cm

in model scale. The model roof has a 2% slope and 216 pressure taps were connected to the walls and roof of the model to obtain the high-resolution pressure distribution. The low-rise model is shown in

Figure 2, and the pressure taps layout is shown in Figure 3.

### 3.2. Mid-rise Model

The mid-rise model was created after a typical mid-rise building. The model scale was 1:100 for wind-tunnel testing. The full-scale dimensions of the mid-rise building are 60 m (length) × 30 m (width) × 50 m (height). The building model has a flat roof and 512 pressure taps were connected to it. The mid-rise model is shown in Figure 4. The pressure taps layout is shown in Figure 5.

## 4. Terrain

In this study, 50 heterogeneous sites were selected to be simulated in the BLWT. These sites were selected in a way that they were as diverse as possible. These 50 sites were selected among 2116 real-world images, where these 2116 sites were clustered into 50 classes using the k-means algorithm based on the mean and standard deviation of roughness lengths. Ten more sites that experienced the passage of hurricanes were added to the testing. The location and direction of selected sites are summarized in Table 1.

Since the Terraformer has 62 × 18 roughness elements with 0.30 m spacing, we considered an upwind area of 62 × 0.3 m × 100 (1/scale factor) = 1860 m by 18 × 0.3 m × 100 (1/scale factor) = 540 m. Similarly, for the 1:50 scale factor, we used an upwind area of 930 m × 270 m. These sites had different land coverage and different roughness changes. Some examples of the selected sites are shown in Figure 6. To convert the land coverage to roughness length, each image was converted to a $z_0$ map based on Table 2. For sites 1 to 5, we produced three different $z_0$ maps for each site using the maximum, average and minimum $z_0$ values in last column of Table 2. For sites 6 to 50,

one $z_0$ map was created based on the average $z_0$ value. For the 10 sites that were selected based on past hurricanes, two different $z_0$ maps for each site using the maximum and minimum $z_0$ values were produced. Also, one uniform case was considered for these 10 sites. Then, Eq. 1 (Macdonald et al., 1998) was utilized to obtain the height of roughness elements. For all cases, the wide edge of roughness elements faced the flow in BLWT.

$$\frac{z_0}{H} = \left(1 - \frac{d}{H}\right) \exp\left[-\left\{0.5 \frac{C_D}{\kappa^2}\left(1 - \frac{d}{H}\right)^{-0.5}\right\}\right] \quad (1)$$

where $H$ is the height of the roughness elements, $C_D$ is the drag coefficient, which is equal to 1.2 based on the face of a cube over shear flow (Macdonald et al., 1998), $\kappa$ is von Kármán's constant, and $\frac{d}{H} = 1 + \Phi^{-\lambda}(\lambda - 1)$, where λ is the total plane area of the whole array of obstacles over the total area of upwind fetch, which is equal to 0.0555 in the UF's BLWT, and $\Phi$ is a constant parameter equal to 4.43 for staggered configuration of roughness elements (Fernández-Cabán and Masters 2017).

# 5. Wind Speed Testing Data Presentations

## 5.1. Wind Profile for 1:50 Geometric Scale

For wind speed testing, 90 cases were simulated in the BLWT with a 1:50 geometric scale. The name and details of each case are summarized in Table 3. CSV files in the specified path were introduced to the BLWT to simulate the upwind terrain. Each cell in the CSV files is the height of the roughness elements in centimeters. CSV files in set A corresponded to the 10 sites that experienced past hurricanes and sets B, C, and D corresponded to the 50 heterogeneous sites in the 1:50 geometric scale. The duration of testing for sets A, B, and C was 45 seconds, while for set D, it was 360 seconds. In set C, the Cobra probes were moved laterally to measure the wind velocity

This file is the final accepted version of the manuscript, published in
https://doi.org/10.1061/JSENDH.STENG-12684

at five different lateral locations. The naming of CSV files in Table 3 follows the site IDs in Table 1. The Max, Min, and Avg configurations refer to maximum, minimum, and average $z_0$ values in Table 2, respectively. As mentioned earlier, for sites 6 to 50, only the Avg configuration was tested.

### 5.2. Wind Profile for 1:100 Geometric Scale

Same as the previous section, 90 cases were simulated in the BLWT with a 1:100 geometric scale. The name and details of each case are summarized in Table 4. CSV files in the sets A to D corresponded to the same sites as the previous section but in a 1:100 geometric scale. The duration of testing for sets A, B, and C was the same as the previous section, but for set D, it was 240 seconds. The naming convention in Table 4 is the same as in Table 3, but here the scale is 1:100.

### 5.3. Validation of Wind Speed Measurements

To validate the wind speed measurement, the wind speed profile and turbulence intensity for 10 different nonuniform cases were compared with two different uniform cases from Alinejad et al., (2023) with $H$ = 33 and 109 mm and wide edge orientation of roughness elements, as shown in Figures 8 and 9. The results shows that nonuniform cases were bounded between two uniform cases with $z_0$ = 0.08 m for $H$= 33 mm and $z_0$ = 1.02 m for $H$= 109 mm.

Also, the wind speed power spectra of 3 cases in the wind tunnel are plotted in Figure 10. The small grey dots show the power spectra from the longitudinal wind speed measurement in the wind tunnel using Pwelch function and the solid thin black curve is the bin average of power spectra. The solid thick line is the empirical model described by Eq.2 (ESDU, 1974).

$$\frac{nS_{uu}}{\sigma_u^2} = \frac{4f}{(1+70.8f^2)^{5/6}} \tag{2}$$

where $n$ is the frequency in Hertz, $S_{uu}$ is the power spectrum for the longitudinal turbulence component, $\sigma_u$ is the standard deviation of the longitudinal velocity component and $f = nL_{ux}/U_z$ in which $L_{ux}$ is the longitudinal integral length scale.

The power spectra plots show a good match between the ESDU model (Eq.3) and wind tunnel results. However, the fluctuation of power spectra is too much and needs to be further investigated.

The effective $z_0$ was estimated after the testing for both 1:50 and 1:100 scales using the log-law method described in Catarelli et al. (2020) and Fernández-Cabán & Masters (2017), which is shown in Figure 11. The longitudinal length scale is plotted in Figure 12 for cases in sets B, C, and D with 1:100 and 1:50 scales at 10 m height. The average longitudinal integral length scale at 10 m height was 1.038 m in the 1:100 scale (103.8 m in full scale) and 1.314 m in the 1:50 scale (65.7 m in full scale). To compare the wind tunnel integral length scale with the field measurements, the results of field measurements from Tieleman (2003) show that at 10 m height, the longitudinal length scale under slightly steady night time condition was 51 m and under unstable day time condition was 190 m. Detailed analysis of wind speed measurements is available in An et al., (2023).

# 6. Wind Pressure Testing Data Presentations

## 6.1. Wind Pressure Coefficients for Low-rise Building Model

To obtain the pressure on the low-rise building model, 60 generic heterogeneous upwind terrain configurations were simulated in the BLWT. The reference velocity for each case was measured at the model's eave height (7.9 cm). Due to the model's symmetry, the wind angle of attack altered from 0 to 90 degrees with a 15-degree increment. More details on this part of the experiment are in Table 5. The duration of data collection for upwind terrain configurations in sets B and C was 75 seconds, and for set D was 360 seconds. The channel and module (ZOC) numbers for 216 taps are provided in the Matlab pressure files under 'TapData' structure array. The name of the pressure tap in the 'TapData' should match the name in the Matlab data file. For example, module (ZOC)

number 2, channel number 39 refers to tap 401 located on surface number 6 at x= -32.25 mm, y = -103.75 mm, and z = 80.48 mm. In the Matlab pressure data file, 'ZOC 2, Channel 39' was stored in column 49 of 'Headers.' Therefore, the differential pressure data for this tap can be accessed in column 49 of 'PressDyn' structure array. The variables in the Matlab files that stored the pressure data and metadata are described in Table 6. The accessibility of the Matlab files mentioned here is described in section 7. Note that the pressure data in 'Pressraw' array is the total uncorrected pressure, in 'PressTotal' array is the total corrected pressure and in 'PressDyn' array is the differential corrected pressure.

### 6.2. Wind Pressure Coefficients for Mid-rise Building Model

60 generic heterogeneous upwind terrain configurations with the 1:100 scale were simulated in the BLWT in front of the mid-rise building model for pressure testing. The reference velocity for each case was measured at the model's roof height (50 cm). The duration of data collection for upwind terrain configurations in sets B and C was 45 seconds, and for set D was 240 seconds. More details on this part of the experiment are in Table 7.

### 6.3. Validation of Wind Pressure Measurements

Here, we plotted the mean pressure coefficient distribution on the low-rise building roof in Figure 13. Figure 13a shows the result of testing by Fernández-Cabán & Masters (2018) on the same low-rise building under uniform upwind terrains. The height of roughness elements (H) was 60 mm with wide edge configuration and the angle of attack is 0 degree in Figure 13a. Figure 13b shows the mean pressure coefficient distribution on the roof of the low-rise model for the site03-Avg case. Note that since the results of uniform cases were low-pass filtered with a cut-off frequency of 300 Hz, we applied the same filter in Figure 13 to the nonuniform terrain to plot the pressure coefficients. We observed that both cases had the same pattern of pressure distributions. However, there was between a 20 and 50 % increase in the mean pressure coefficient when the nonuniform

This file is the final accepted version of the manuscript, published in
https://doi.org/10.1061/JSENDH.STENG-12684

upwind terrain was tested which can be related to the nonuniform simulation of upwind terrain and non-equilibrium state of the wind flow.

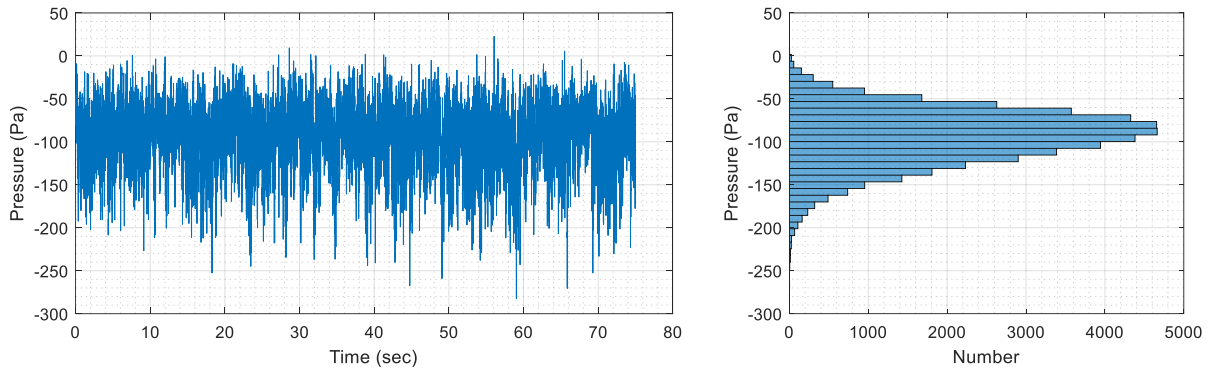


(a) (b)

Figure 14 shows the time history and histogram of the corrected differential pressure ('PressDyn' array) on the tap number 401 located on the low-rise model's roof (x= -32.25 mm and y= -103.75 mm) where the average pressure is -94.9 Pa with standard deviation of 32.7, skewness of -0.51 and kurtosis of 3.5.

The results of testing on TTU building model on uniform upwind terrains (Fernández-Cabán & Masters, 2018a) for the ridge of the roof and the same results from BLWT tests were plotted in Figure 15, which shows a good match in general. We plotted 2 different uniform cases from Fernández-Cabán & Masters's (2018a) dataset, wide edge uniform configuration of roughness elements with 10 mm and 100 mm heights. Both tests were performed on the exact same model with 1:50 scale. However, the duration of tests on uniform cases was 120 seconds. The simple worst method (Gavanski & Uematsu, 2014) was used in the peak pressure analysis in Figure 15.

To further discuss the pressure distribution, we plotted the minimum of mean pressure coefficients (absolute maximum of Cp-mean) along the ridge of the roof for the low-rise model in Figure 16.

This file is the final accepted version of the manuscript, published in
https://doi.org/10.1061/JSENDH.STENG-12684

In Figure 16, the nonuniform cases are all 60 cases in Table 5 and the uniform cases are 17 uniform cases with $H$= 0 mm up to 160 cm from Fernández-Cabán & Masters's (2018) dataset with wide edge uniform configuration of roughness when the angle of attack was zero. It's apparent from Figure 16 that the pressure coefficient is related to the turbulence intensity. Here, we observed that in the nonuniform cases with small turbulence intensity ($I_u$ < 0.15), the minimum of pressure coefficients along the ridge was close to uniform cases. However, in larger turbulence intensity regions ($I_u$ > 0.2), with the same $I_u$, nonuniform cases produced larger suction than uniform ones, and differences between nonuniform and uniform cases increased with the increase in turbulence intensity.

Figure 17 shows the mean pressure coefficient distribution on the mid-rise building for site 15 with 90 degrees angle of attack. Note that in the low-rise model, all pressure taps in module 6 had a malfunction for the following sites: site 1-Max, angle of attack 90; site 2-Avg, angles of attack 0, 30 and 90; site 2-Min, angle of attack 30; site 3-Max, angle of attack 60 and 75; site 3-Min, angle of attack 90; site 5-min, angle of attack 0 and 15; site 17-Avg, angle of attack 75; site 23-Avg, angle of attack 75; site 30-Avg, angle of attack 45; site 32-Avg, angle of attack 30; site 38-Avg, angle of attack 45, 60, 75 and 90; site 40-Avg, angle of attack 60; and site 47-Avg, angle of attack 30. Also, note that in the mid-rise model, 14 pressure taps out of 512 taps had a malfunction and should be excluded from the results. These malfunctioned taps are module 1, channels 57 to 64; module 5, channels 54, 55, 62 and 64; and module 8, channels 54 and 55.

## 7. Data Organization

Figure 18 shows how the data and metadata files can be accessed through the DesignSafe-CI repository. The data files were stored in three folders, the 'EVT01' folder stored the wind speed

measurement files, and the 'EVT02' and 'EVT03' folders stored the wind pressure measurement files for low-rise and mid-rise building models, respectively. In the 'EVT01' folder, there are two subfolders with 180 folders in each referring to wind speed MATLAB data files and photos of the Terraformer named after the first column of Table 3 and Table 4. There are three subfolders in the 'EVT02' and 'EVT03' folders. The 'Cobra Probe' folder stores the reference velocity measurements. The 'Scanivalve' folder stores the pressure measurements where the pressure data MATLAB files were named after Table 5 or Table 7 (low-rise or mid-rise) following the angle of attack. The photos of building models in front of the Terraformer are stored in the 'Photos' folder. The input CSV files for two different scales are stored in the 'Terrain configuration' folder. The pressure taps layout, coordination, and names are also stored in the two excel files in the 'Documents' folder.

## 8. Discussion and Conclusion

This study aimed to first provide an experimental dataset of wind speed measurement for 180 upwind terrain configurations in the BLWT at UF NEHRI-EF. The upwind terrain dataset consists of 50 real-world generic heterogeneous terrains which had different land coverage combinations and 10 upwind terrains that experienced the passage of hurricanes. This part of the experiment can be used to investigate the effect of upwind terrain on wind characteristics such as wind profile and turbulence intensity. The results can be compared to the previous models, such as Deaves and Harris model (Cook, 1997; Deaves, 1980, 1981) and the model proposed by Wang & Stathopoulos (2007) and to propose a model to predict the wind profile for different combinations of land coverages.

The second objective of this study was to provide an accessible dataset to investigate further the effect of heterogeneous upwind terrain on wind loads on two different building models. The upwind terrain configuration simulated in the BLWT consists of 50 real-world generic heterogeneous terrains. The results can be used to develop a neural network model that can predict the pressure distribution given the characteristics of upwind terrain and wind flow as well as validate the numerical models such as CFD models.

It is important to mention that there is a roughness change between the model and the first raw of roughness elements (2 m gap) since the turntable in front of the Terraformer would not allow the roughness elements to be there. Also, this study did not consider any surrounding buildings near the installed building models. The dimension of the upwind Terrain simulated in the wind tunnel was limited to the dimension of upwind fetch (Terraformer), which was 1860 m × 540 m in 1:100 scale and 930 m × 270 m in 1:50 scale. Moreover, the scaling issue and Reynolds number and their effects on the pressure loading can be further assessed.

## Data Availability

The data and metadata are publicly available on the DesignSafe-CI repository under the DOI of 10.17603/Ds2-6hg9-R131.

## Acknowledgments

This material is based upon work supported by the National Science Foundation under Grant No. CMMI-1856205. Any opinions, findings, and conclusions or recommendations expressed in this

material are those of the authors and do not necessarily reflect the views of the National Science Foundation.

# References

Alinejad, N., Jung, S., Kakareko, G., & Fernández-Cában, P. L. (2023). Wind-Tunnel Reproduction of Nonuniform Terrains Using Local Roughness Zones. *Boundary-Layer Meteorology*, *188*(3), 463–484. https://doi.org/10.1007/s10546-023-00822-0

An, L.-S., Alinejad, N., Kim, S., & Jung, S. (2023). Experimental study on wind characteristics and prediction of mean wind profile over complex heterogeneous terrain. *Building and Environment*, 110719. https://doi.org/10.1016/j.buildenv.2023.110719

Balderrama, J. A., Masters, F. J., & Gurley, K. R. (2012). Peak factor estimation in hurricane surface winds. *Journal of Wind Engineering and Industrial Aerodynamics*, *102*, 1–13. https://doi.org/10.1016/j.jweia.2011.12.003

Catarelli, R. A., Fernández-Cabán, P. L., Masters, F. J., Bridge, J. A., Gurley, K. R., & Matyas, C. J. (2020). Automated terrain generation for precise atmospheric boundary layer simulation in the wind tunnel. *Journal of Wind Engineering and Industrial Aerodynamics*, *207*, 104276. https://doi.org/10.1016/j.jweia.2020.104276

Chen, B., Shang, L., Qin, M., Chen, X., & Yang, Q. (2018). Wind interference effects of high-rise building on low-rise building with flat roof. *Journal of Wind Engineering and Industrial Aerodynamics*, *183*(March), 88–113. https://doi.org/10.1016/j.jweia.2018.10.019

Cheung, J. C. K., Holmes, J. D., Melbourne, W. H., Lakshmanan, N., & Bowditch, P. (1997). Pressures on a scale model of the Texas Tech Building. *Journal of Wind Engineering and Industrial Aerodynamics*, *69–71*, 529–538. https://doi.org/10.1016/S0167-6105(97)00183-9

Cook, N. J. (1997). The Deaves and Harris ABL Model Applied To Heterogeneous Terrain. *Journal of Wind Engineering and Industrial Aerodynamics*, *66*, 197–214.

Davenport, A. G. (1960). Wind loads on structures. In *National research council, canads, division of building research*.

Deaves, D. M. (1980). Computations of wind flow over two-dimensional hills and embankments. *Journal of Wind Engineering and Industrial Aerodynamics*, *6*(1–2), 89–111. https://doi.org/10.1016/0167-6105(80)90024-0

Deaves, D. M. (1981). Computations of wind flow over changes in surface roughness. *Journal of Wind Engineering and Industrial Aerodynamics*, *7*(1), 65–94. https://doi.org/10.1016/0167-6105(81)90068-4

ESDU. (1974). Characteristics of atmospheric turbulence near the ground. Part I: definitions and general information. *Engineering Sciences Data Unit, Itm. No. 7*(London, UK).

Fernández-Cabán, P.L., & Masters, F. J. (2017). Near surface wind longitudinal velocity positively skews with increasing aerodynamic roughness length. *Journal of Wind Engineering and Industrial Aerodynamics*, *169*, 94–105. https://doi.org/10.1016/j.jweia.2017.06.007

Fernández-Cabán, Pedro L., & Masters, F. J. (2018). Behavior of Hurricane Wind and Wind-Driven Rain in the Coastal Suburban Roughness Sublayer. *DesignSafe-CI*. https://doi.org/10.17603/DS2110K

Fernández-Cabán, Pedro L., & Masters, F. J. (2020). Experiments in a Large Boundary Layer Wind Tunnel: Upstream Terrain Effects on Surface Pressures Acting on a Low-Rise Structure. *Journal of Structural Engineering*, *146*(8), 04720002. https://doi.org/10.1061/(ASCE)ST.1943-541X.0002690

Gavanski, E., & Uematsu, Y. (2014). Local wind pressures acting on walls of low-rise buildings and comparisons to the Japanese and US wind loading provisions. *Journal of Wind Engineering and Industrial Aerodynamics*, *132*, 77–91. https://doi.org/10.1016/j.jweia.2014.06.020

He, Y. C., Chan, P. W., & Li, Q. S. (2017). Estimation of roughness length at Hong Kong International Airport via different micrometeorological methods. *Journal of Wind Engineering and Industrial Aerodynamics*, *171*(September), 121–136. https://doi.org/10.1016/j.jweia.2017.09.019

Kopp, G. A., Surry, D., & Mans, C. (2005). Wind effects of parapets on low buildings: Part 1. Basic aerodynamics and local loads. *Journal of Wind Engineering and Industrial Aerodynamics*, *93*(11), 817–841. https://doi.org/10.1016/j.jweia.2005.08.006

Levitan, M. L., & Mehta, K. C. (1992). Texas Tech field experiments for wind loads part 1: building and pressure measuring system. *Journal of Wind Engineering and Industrial Aerodynamics*, *43*(1–3), 1565–1576. https://doi.org/10.1016/0167-6105(92)90372-H

Lim, H. C., Tsukamoto, K., Ohba, M., & Mizutani, K. (2014). Study on the surface pressure distribution of cubes in cross-wind arrays. *Journal of Wind Engineering and Industrial Aerodynamics*, *133*, 18–26. https://doi.org/10.1016/j.jweia.2014.07.009

Macdonald, R. ., Griffiths, R. ., & Hall, D. . (1998). An improved method for the estimation of surface roughness of obstacle arrays. *Atmospheric Environment*, *32*(11), 1857–1864. https://doi.org/10.1016/S1352-2310(97)00403-2

Sabareesh, G.R., Matsui, M., & Tamura, Y. (2013). Characteristics of internal pressures and net local roof wind forces on a building exposed to a tornado-like vortex. *Journal of Wind Engineering and Industrial Aerodynamics*, *112*, 52–57. https://doi.org/10.1016/j.jweia.2012.11.005

Tieleman, H. W. (2003). Wind tunnel simulation of wind loading on low-rise structures: a review. *Journal of Wind Engineering and Industrial Aerodynamics*, *91*(12–15), 1627–1649. https://doi.org/10.1016/j.jweia.2003.09.021

Vihma, T., & Savijärvi, H. (1991). On the effective roughness length for heterogeneous terrain. *Quarterly Journal of the Royal Meteorological Society*, *117*(498), 399–407. https://doi.org/10.1002/qj.49711749808

Wang, K., & Stathopoulos, T. (2007). Exposure model for wind loading of buildings. *Journal of Wind Engineering and Industrial Aerodynamics*, *95*(9–11), 1511–1525. https://doi.org/10.1016/j.jweia.2007.02.016

Wang, Kai, & Stathopoulos, T. (2006). The impact of exposure on wind loading of low buildings. *Proceedings of the Structures Congress and Exposition*, *2006*, 9. https://doi.org/10.1061/40889(201)9

Wiernga, J. (1993). Representative roughness parameters for homogeneous terrain. *Boundary-Layer Meteorology*, *63*(4), 323–363. https://doi.org/10.1007/BF00705357

Zisis, I., & Stathopoulos, T. (2010). Wind loads on low-rise buildings: Upstream exposure effect. *7th Asia-Pacific Conf. on Wind Engineering*.

This file is the final accepted version of the manuscript, published in
https://doi.org/10.1061/JSENDH.STENG-12684

# Tables

Table 1: Information on selected sites to be tested in the BLWT

| Site ID | Latitude | Longitude | Direction from magnetic north | Site ID | Latitude | Longitude | Direction from magnetic north |
|---|---|---|---|---|---|---|---|
| 1 | 30.68526 | -88.0254 | 0 | 31 | 38.06936 | -75.5499 | 90 |
| 2 | 27.6763 | -97.2861 | 270 | 32 | 41.20402 | -73.0934 | 90 |
| 3 | 43.18735 | -77.6305 | 90 | 33 | 36.0522 | -86.8092 | 270 |
| 4 | 30.41956 | -84.318 | 0 | 34 | 34.44947 | -77.5262 | 90 |
| 5 | 44.24718 | -72.5886 | 90 | 35 | 41.38552 | -71.494 | 180 |
| 6 | 41.7158 | -73.9159 | 180 | 36 | 37.67902 | -75.6308 | 90 |
| 7 | 38.06936 | -75.5499 | 180 | 37 | 38.72918 | -90.4551 | 90 |
| 8 | 33.67731 | -79.0314 | 0 | 38 | 25.41191 | -80.4964 | 270 |
| 9 | 30.22528 | -92.0613 | 90 | 39 | 31.59068 | -83.2424 | 0 |
| 10 | 41.02429 | -73.6259 | 90 | 40 | 43.62806 | -72.5149 | 270 |
| 11 | 31.06005 | -81.4208 | 0 | 41 | 34.93197 | -81.0286 | 270 |
| 12 | 33.89831 | -78.4307 | 270 | 42 | 40.76147 | -73.4698 | 0 |
| 13 | 38.45491 | -75.058 | 90 | 43 | 37.79596 | -80.2998 | 180 |
| 14 | 42.87553 | -71.9509 | 270 | 44 | 40.6656 | -73.9868 | 90 |
| 15 | 36.76553 | -76.3582 | 90 | 45 | 30.2068 | -93.2414 | 180 |
| 16 | 30.4202 | -81.5567 | 90 | 46 | 37.6916 | -75.7141 | 0 |
| 17 | 38.20711 | -75.6946 | 0 | 47 | 39.05953 | -84.6102 | 90 |
| 18 | 35.67342 | -105.911 | 90 | 48 | 38.72754 | -75.2634 | 0 |
| 19 | 39.90773 | -75.1917 | 0 | 49 | 30.28072 | -87.5809 | 270 |
| 20 | 31.20489 | -85.4051 | 180 | 50 | 44.32527 | -69.7537 | 0 |
| 21 | 30.50375 | -89.6601 | 270 | SandyT3-d60 | 39.3208 | -74.5953 | 60 |
| 22 | 39.8525 | -88.906 | 0 | MatthewT3FL-d170 | 28.1937 | -80.6056 | 200 |
| 23 | 30.26644 | -89.415 | 0 | IrmaT2-d250 | 26.3304 | -81.7791 | 250 |
| 24 | 34.81752 | -82.4157 | 180 | IsaacT2-d170 | 29.5385 | -89.7751 | 170 |

| | | | | | | | |
|---|---|---|---|---|---|---|---|
| 25 | 36.75083 | -96.0075 | 270 | IsaacT2-d25 | 29.5385 | -89.7751 | 25 |
| 26 | 41.33751 | -71.7566 | 180 | ArthurT2-d35 | 35.2322 | -75.6215 | 35 |
| 27 | 37.73784 | -88.946 | 90 | ArthurT2-d80 | 35.2322 | -75.6215 | 80 |
| 28 | 37.96214 | -91.7524 | 0 | ArthurT2-d155 | 35.2322 | -75.6215 | 155 |
| 29 | 31.07034 | -81.4076 | 180 | HarveyT2-d200 | 35.2322 | -75.6215 | 200 |
| 30 | 32.9042 | -79.9706 | 0 | HarveyT3-d80 | 28.6119 | -96.6252 | 80 |

Table 2: Terrain classifications and $z_0$ range ($z_0$ range is based on Davenport 1960; Vihma and Savijärvi 1991; Wieringa 1993; Wang and Stathopoulos 2007; He et al., 2017)

| Terrain description | $z_0$ range (m) |
|---|---|
| Water (river, sea, lake, etc.) | 0.0001-0.0005 |
| Featureless Land | 0.001-0.005 |
| Road | 0.0024-0.03 |
| Short Grass | 0.001-0.03 |
| Low-rise Building | 0.3-0.7 |
| Mid-rise Building | 0.5-1.5 |
| Forest | 1- 2.3 |

Table 3: Details of testing for wind speed profile with 1:50 scale

| Profile name | CSV file path | CSV file name | Cobra probes' location(s) |
|---|---|---|---|
| 0030301S0001 | Low-Rise\set A | SandyT3-d60-Nonuniform-Max-50 | X= 2950 cm, Y= 0.00 |
| 0030301S0002 | Low-Rise\set A | SandyT3-d60-Nonuniform-Min-50 | X= 2950 cm, Y= 0.00 |
| 0030301S0003 | Low-Rise\set A | SandyT3-d60-Uniform-Min-50 | X= 2950 cm, Y= 0.00 |
| 0030301S0004 | Low-Rise\set A | MatthewT3FL-d170-Nonuniform-Max-50 | X= 2950 cm, Y= 0.00 |
| 0030301S0005 | Low-Rise\set A | MatthewT3FL- d170-Nonuniform-Min-50 | X= 2950 cm, Y= 0.00 |
| 0030301S0006 | Low-Rise\set A | MatthewT3FL- d170-Uniform-Min-50 | X= 2950 cm, Y= 0.00 |
| 0030301S0007 | Low-Rise\set A | IrmaT2-d250-Nonuniform-Max-50 | X= 2950 cm, Y= 0.00 |
| 0030301S0008 | Low-Rise\set A | IrmaT2-d250-Nonuniform-Min-50 | X= 2950 cm, Y= 0.00 |
| 0030301S0009 | Low-Rise\set A | IrmaT2-d250-Uniform-Min-50 | X= 2950 cm, Y= 0.00 |
| 0030301S0010 | Low-Rise\set A | IsaacT2-d170-Nonuniform-Max-50 | X= 2950 cm, Y= 0.00 |
| 0030301S0011 | Low-Rise\set A | IsaacT2-d170-Nonuniform-Min-50 | X= 2950 cm, Y= 0.00 |
| 0030301S0012 | Low-Rise\set A | IsaacT2-d170-Uniform-Min-50 | X= 2950 cm, Y= 0.00 |
| 0030301S0013 | Low-Rise\set A | IsaacT2-d25-Nonuniform-Max-50 | X= 2950 cm, Y= 0.00 |
| 0030301S0014 | Low-Rise\set A | IsaacT2-d25-Nonuniform-Min-50 | X= 2950 cm, Y= 0.00 |
| 0030301S0015 | Low-Rise\set A | IsaacT2-d25-Uniform-Min-50 | X= 2950 cm, Y= 0.00 |
| 0030301S0016 | Low-Rise\set A | ArthurT2-d35-Nonuniform-Max-50 | X= 2950 cm, Y= 0.00 |
| 0030301S0017 | Low-Rise\set A | ArthurT2-d35-Nonuniform-Min-50 | X= 2950 cm, Y= 0.00 |
| 0030301S0018 | Low-Rise\set A | ArthurT2-d35-Uniform-Min-50 | X= 2950 cm, Y= 0.00 |
| 0030301S0019 | Low-Rise\set A | ArthurT2-d80-Nonuniform-Max-50 | X= 2950 cm, Y= 0.00 |
| 0030301S0020 | Low-Rise\set A | ArthurT2-d80-Nonuniform-Min-50 | X= 2950 cm, Y= 0.00 |
| 0030301S0021 | Low-Rise\set A | ArthurT2-d80-Uniform-Min-50 | X= 2950 cm, Y= 0.00 |
| 0030301S0022 | Low-Rise\set A | ArthurT2-d155-Nonuniform-Max-50 | X= 2950 cm, Y= 0.00 |
| 0030301S0023 | Low-Rise\set A | ArthurT2-d155-Nonuniform-Min-50 | X= 2950 cm, Y= 0.00 |
| 0030301S0024 | Low-Rise\set A | ArthurT2-d155-Uniform-Min-50 | X= 2950 cm, Y= 0.00 |
| 0030301S0025 | Low-Rise\set A | HarveyT2-d200-Nonuniform-Max-50 | X= 2950 cm, Y= 0.00 |
| 0030301S0026 | Low-Rise\set A | HarveyT2-d200-Nonuniform-Min-50 | X= 2950 cm, Y= 0.00 |
| 0030301S0027 | Low-Rise\set A | HarveyT2-d200 -Uniform-Min-50 | X= 2950 cm, Y= 0.00 |

This file is the final accepted version of the manuscript, published in
https://doi.org/10.1061/JSENDH.STENG-12684

| | | | |
|---|---|---|---|
| 0030301S0028 | Low-Rise\set A | HarveyT3-d80-Nonuniform-Max-50 | X= 2950 cm, Y= 0.00 |
| 0030301S0029 | Low-Rise\set A | HarveyT3-d80-Nonuniform-Min-50 | X= 2950 cm, Y= 0.00 |
| 0030301S0030 | Low-Rise\set A | HarveyT3-d80-Uniform-Min-50 | X= 2950 cm, Y= 0.00 |
| 0030301S0031 | Low-Rise\set B | Low-Site01-Avg | X= 2950 cm, Y= 0.00 |
| 0030301S0032 | Low-Rise\set B | Low-Site01-Max | X= 2950 cm, Y= 0.00 |
| 0030301S0033 | Low-Rise\set B | Low-Site01-Min | X= 2950 cm, Y= 0.00 |
| 0030301S0034 | Low-Rise\set B | Low-Site02-Avg | X= 2950 cm, Y= 0.00 |
| 0030301S0035 | Low-Rise\set B | Low-Site02-Max | X= 2950 cm, Y= 0.00 |
| 0030301S0036 | Low-Rise\set B | Low-Site02-Min | X= 2950 cm, Y= 0.00 |
| 0030301S0037 | Low-Rise\set B | Low-Site03-Avg | X= 2950 cm, Y= 0.00 |
| 0030301S0038 | Low-Rise\set B | Low-Site03-Max | X= 2950 cm, Y= 0.00 |
| 0030301S0039 | Low-Rise\set B | Low-Site03-Min | X= 2950 cm, Y= 0.00 |
| 0030301S0040 | Low-Rise\set B | Low-Site04-Avg | X= 2950 cm, Y= 0.00 |
| 0030301S0041 | Low-Rise\set B | Low-Site04-Max | X= 2950 cm, Y= 0.00 |
| 0030301S0042 | Low-Rise\set B | Low-Site04-Min | X= 2950 cm, Y= 0.00 |
| 0030301S0043 | Low-Rise\set B | Low-Site05-Avg | X= 2950 cm, Y= 0.00 |
| 0030301S0044 | Low-Rise\set B | Low-Site05-Max | X= 2950 cm, Y= 0.00 |
| 0030301S0045 | Low-Rise\set B | Low-Site05-Min | X= 2950 cm, Y= 0.00 |
| 0030301S0046 to 0030301S0075 | Low-Rise\set B | Low-Site06 to Low-Site35 | X= 2950 cm, Y= 0.00 |
| 0030301S0076 to 0030301S0085 | Low-Rise\set C | Low-Site36 to Low-Site45 | X= 2950 cm, Y= [0.00, ±30, ±60 cm] |
| 0030301S0086 to 0030301S0090 | Low-Rise\set D | Low-Site46 to Low-Site50 | X= 2950 cm, Y= 0.00 |

383

384 Table 4: Details of testing for wind speed profile with 1:100 scale

| Profile name | CSV file path | CSV file name | Cobra probes' location(s) |
|---|---|---|---|
| 0030301S0091 | Mid-Rise\set A | SandyT3-d60-Nonuniform-Max-100 | X= 2950 cm, Y= 0.00 |
| 0030301S0092 | Mid-Rise\set A | SandyT3-d60-Nonuniform-Min-100 | X= 2950 cm, Y= 0.00 |
| 0030301S0093 | Mid-Rise\set A | SandyT3-d60-Uniform-Min-100 | X= 2950 cm, Y= 0.00 |
| 0030301S0094 | Mid-Rise\set A | MatthewT3FL-d170-Nonuniform-Max-100 | X= 2950 cm, Y= 0.00 |
| 0030301S0095 | Mid-Rise\set A | MatthewT3FL- d170-Nonuniform-Min-100 | X= 2950 cm, Y= 0.00 |
| 0030301S0096 | Mid-Rise\set A | MatthewT3FL- d170-Uniform-Min-100 | X= 2950 cm, Y= 0.00 |
| 0030301S0097 | Mid-Rise\set A | IrmaT2-d250-Nonuniform-Max-100 | X= 2950 cm, Y= 0.00 |
| 0030301S0098 | Mid-Rise\set A | IrmaT2-d250-Nonuniform-Min-100 | X= 2950 cm, Y= 0.00 |
| 0030301S0099 | Mid-Rise\set A | IrmaT2-d250-Uniform-Min-100 | X= 2950 cm, Y= 0.00 |
| 0030301S0100 | Mid-Rise\set A | IsaacT2-d170-Nonuniform-Max-100 | X= 2950 cm, Y= 0.00 |
| 0030301S0101 | Mid-Rise\set A | IsaacT2-d170-Nonuniform-Min-100 | X= 2950 cm, Y= 0.00 |
| 0030301S0102 | Mid-Rise\set A | IsaacT2-d170-Uniform-Min-100 | X= 2950 cm, Y= 0.00 |
| 0030301S0103 | Mid-Rise\set A | IsaacT2-d25-Nonuniform-Max-100 | X= 2950 cm, Y= 0.00 |
| 0030301S0104 | Mid-Rise\set A | IsaacT2-d25-Nonuniform-Min-100 | X= 2950 cm, Y= 0.00 |
| 0030301S0105 | Mid-Rise\set A | IsaacT2-d25-Uniform-Min-100 | X= 2950 cm, Y= 0.00 |
| 0030301S0106 | Mid-Rise\set A | ArthurT2-d35-Nonuniform-Max-100 | X= 2950 cm, Y= 0.00 |
| 0030301S0107 | Mid-Rise\set A | ArthurT2-d35-Nonuniform-Min-100 | X= 2950 cm, Y= 0.00 |
| 0030301S0108 | Mid-Rise\set A | ArthurT2-d35-Uniform-Min-100 | X= 2950 cm, Y= 0.00 |
| 0030301S0109 | Mid-Rise\set A | ArthurT2-d80-Nonuniform-Max-100 | X= 2950 cm, Y= 0.00 |
| 0030301S0110 | Mid-Rise\set A | ArthurT2-d80-Nonuniform-Min-100 | X= 2950 cm, Y= 0.00 |
| 0030301S0111 | Mid-Rise\set A | ArthurT2-d80-Uniform-Min-100 | X= 2950 cm, Y= 0.00 |
| 0030301S0112 | Mid-Rise\set A | ArthurT2-d155-Nonuniform-Max-100 | X= 2950 cm, Y= 0.00 |

| | | | |
|---|---|---|---|
| 0030301S0113 | Mid-Rise\set A | ArthurT2-d155-Nonuniform-Min-100 | X= 2950 cm, Y= 0.00 |
| 0030301S0114 | Mid-Rise\set A | ArthurT2-d155-Uniform-Min-100 | X= 2950 cm, Y= 0.00 |
| 0030301S0115 | Mid-Rise\set A | HarveyT2-d200-Nonuniform-Max-100 | X= 2950 cm, Y= 0.00 |
| 0030301S0116 | Mid-Rise\set A | HarveyT2-d200-Nonuniform-Min-100 | X= 2950 cm, Y= 0.00 |
| 0030301S0117 | Mid-Rise\set A | HarveyT2-d200 -Uniform-Min-100 | X= 2950 cm, Y= 0.00 |
| 0030301S0118 | Mid-Rise\set A | HarveyT3-d80-Nonuniform-Max-100 | X= 2950 cm, Y= 0.00 |
| 0030301S0119 | Mid-Rise\set A | HarveyT3-d80-Nonuniform-Min-100 | X= 2950 cm, Y= 0.00 |
| 0030301S0120 | Mid-Rise\set A | HarveyT3-d80-Uniform-Min-100 | X= 2950 cm, Y= 0.00 |
| 0030301S0121 | Mid-Rise\set B | Mid-Site01-Avg | X= 2950 cm, Y= 0.00 |
| 0030301S0122 | Mid-Rise\set B | Mid-Site01-Max | X= 2950 cm, Y= 0.00 |
| 0030301S0123 | Mid-Rise\set B | Mid-Site01-Min | X= 2950 cm, Y= 0.00 |
| 0030301S0124 | Mid-Rise\set B | Mid-Site02-Avg | X= 2950 cm, Y= 0.00 |
| 0030301S0125 | Mid-Rise\set B | Mid-Site02-Max | X= 2950 cm, Y= 0.00 |
| 0030301S0126 | Mid-Rise\set B | Mid-Site02-Min | X= 2950 cm, Y= 0.00 |
| 0030301S0127 | Mid-Rise\set B | Mid-Site03-Avg | X= 2950 cm, Y= 0.00 |
| 0030301S0128 | Mid-Rise\set B | Mid-Site03-Max | X= 2950 cm, Y= 0.00 |
| 0030301S0129 | Mid-Rise\set B | Mid-Site03-Min | X= 2950 cm, Y= 0.00 |
| 0030301S0130 | Mid-Rise\set B | Mid-Site04-Avg | X= 2950 cm, Y= 0.00 |
| 0030301S0131 | Mid-Rise\set B | Mid-Site04-Max | X= 2950 cm, Y= 0.00 |
| 0030301S0132 | Mid-Rise\set B | Mid-Site04-Min | X= 2950 cm, Y= 0.00 |
| 0030301S0133 | Mid-Rise\set B | Mid-Site05-Avg | X= 2950 cm, Y= 0.00 |
| 0030301S0134 | Mid-Rise\set B | Mid-Site05-Max | X= 2950 cm, Y= 0.00 |
| 0030301S0135 | Mid-Rise\set B | Mid-Site05-Min | X= 2950 cm, Y= 0.00 |
| 0030301S0136 to 0030301S0165 | Mid-Rise\set B | Mid-Site06 to Mid-Site35 | X= 2950 cm, Y= 0.00 |
| 0030301S0166 to 0030301S0175 | Mid-Rise\set C | Mid-Site36 to Mid-Site45 | X= 2950 cm, Y= [0.00, ±30, ±60 cm] |
| 0030301S0176 to 0030301S0180 | Mid-Rise\set D | Mid-Site46 to Mid-Site50 | X= 2950 cm, Y= 0.00 |

385

386 Table 5: Details of wind pressure testing for low-rise model

| Pressure name | CSV file path | File name | Reference velocity measurement point | Angle |
|---|---|---|---|---|
| 0030302S0001 | Low-Rise\set B | Low-Site01-Avg | X= 3000 cm, Y= 50 cm, Z= eave height | 0:15:90 |
| 0030302S0002 | Low-Rise\set B | Low-Site01-Max | X= 3000 cm, Y= 50 cm, Z= eave height | 0:15:90 |
| 0030302S0003 | Low-Rise\set B | Low-Site01-Min | X= 3000 cm, Y= 50 cm, Z= eave height | 0:15:90 |
| 0030302S0004 | Low-Rise\set B | Low-Site02-Avg | X= 3000 cm, Y= 50 cm, Z= eave height | 0:15:90 |
| 0030302S0005 | Low-Rise\set B | Low-Site02-Max | X= 3000 cm, Y= 50 cm, Z= eave height | 0:15:90 |
| 0030302S0006 | Low-Rise\set B | Low-Site02-Min | X= 3000 cm, Y= 50 cm, Z= eave height | 0:15:90 |
| 0030302S0007 | Low-Rise\set B | Low-Site03-Avg | X= 3000 cm, Y= 50 cm, Z= eave height | 0:15:90 |
| 0030302S0008 | Low-Rise\set B | Low-Site03-Max | X= 3000 cm, Y= 50 cm, Z= eave height | 0:15:90 |
| 0030302S0009 | Low-Rise\set B | Low-Site03-Min | X= 3000 cm, Y= 50 cm, Z= eave height | 0:15:90 |
| 0030302S0010 | Low-Rise\set B | Low-Site04-Avg | X= 3000 cm, Y= 50 cm, Z= eave height | 0:15:90 |
| 0030302S0011 | Low-Rise\set B | Low-Site04-Max | X= 3000 cm, Y= 50 cm, Z= eave height | 0:15:90 |
| 0030302S0012 | Low-Rise\set B | Low-Site04-Min | X= 3000 cm, Y= 50 cm, Z= eave height | 0:15:90 |
| 0030302S0013 | Low-Rise\set B | Low-Site05-Avg | X= 3000 cm, Y= 50 cm, Z= eave height | 0:15:90 |
| 0030302S0014 | Low-Rise\set B | Low-Site05-Max | X= 3000 cm, Y= 50 cm, Z= eave height | 0:15:90 |
| 0030302S0015 | Low-Rise\set B | Low-Site05-Min | X= 3000 cm, Y= 50 cm, Z= eave height | 0:15:90 |
| 0030302S0016 to | Low-Rise\set B | Low-Site06 to | X= 3000 cm, Y= 50 cm, Z= eave height | 0:15:90 |

This file is the final accepted version of the manuscript, published in
https://doi.org/10.1061/JSENDH.STENG-12684

| | | | | |
|---|---|---|---|---|
| 0030302S0045 | | Low-Site35 | | |
| 0030302S0046 to 0030302S0056 | Low-Rise\set C | Low-Site36 to Low-Site45 | X= 3000 cm, Y= 50 cm, Z= eave height | 0:15:90 |
| 0030302S0056 to 0030302S0060 | Low-Rise\set D | Low-Site46 to Low-Site50 | X= 3000 cm, Y= 50 cm, Z= eave height | 0:15:90 |

387

388 Table 6: Pressure data file variables

| Matlab variables | Description |
|---|---|
| Scanivalve.TimeSeries.Headers | Zoc number and channel number |
| Scanivalve.TimeSeries.Time | Elapsed time (sec) |
| Scanivalve.TimeSeries.SampleRate | Sample rate (Hz) |
| Scanivalve.TimeSeries.PressRaw | Total pressure measured by the Scanivalve system, uncorrected (Pa) |
| Scanivalve.TimeSeries.Press Total | Total pressure corrected for tubing response (Pa) |
| Scanivalve.TimeSeries.PressDyn | Differential pressure corrected for tubing response (Pa) |
| Scanivalve.Reference.Ps | Reference (static) pressure (Pa) |
| Scanivalve.Reference.U | Mean reference longitudinal wind velocity (m/s) |
| Scanivalve.Reference.rho | Air density ($kg/m^3$) |
| Scanivalve.Tube.ind | Integer indicating which tube path corresponds to each tap |
| Scanivalve.Tube.L | Segment length (mm) |
| Scanivalve.Tube.D | Segment inner diameter (mm) |
| Scanivalve.Tube.V_trans | Segment transducer volume ($mm^3$) |
| Scanivalve.TapData (X, Y and Z columns) | Coordinates (X, Y, Z) of pressure taps (mm) |
| Scanivalve. TapData (ZOC33L column) | Length of ZOC connector external tubulation (mm) |
| Scanivalve. TapData (ZOC33D column) | Inner diameter of ZOC connector external tubulation (mm) |
| Scanivalve. TapData (TubeL column) | Length of tube between ZOC connector and model tubulation (mm) |
| Scanivalve. TapData (TubelD column) | Inner diameter of tube between ZOC connector and model tubulation (mm) |
| Scanivalve. TapData (TubulationL column) | Length of model tubulation (mm) |
| Scanivalve. TapData (TubulationlD column) | Inner diameter of model tubulation (mm) |

389

390 Table 7: Details of wind pressure testing for mid-rise model

| Pressure name | CSV file path | File name | Reference velocity measurement point | Angle |
|---|---|---|---|---|
| 0030303S0001 | Mid-Rise\set B | Mid-Site01-Avg | X= 3000 cm, Y= 50 cm, Z= roof height | 0:15:90 |
| 0030303S0002 | Mid-Rise\set B | Mid-Site01-Max | X= 3000 cm, Y= 50 cm, Z= roof height | 0:15:90 |
| 0030303S0003 | Mid-Rise\set B | Mid-Site01-Min | X= 3000 cm, Y= 50 cm, Z= roof height | 0:15:90 |
| 0030303S0004 | Mid-Rise\set B | Mid-Site02-Avg | X= 3000 cm, Y= 50 cm, Z= roof height | 0:15:90 |
| 0030303S0005 | Mid-Rise\set B | Mid-Site02-Max | X= 3000 cm, Y= 50 cm, Z= roof height | 0:15:90 |
| 0030303S0006 | Mid-Rise\set B | Mid-Site02-Min | X= 3000 cm, Y= 50 cm, Z= roof height | 0:15:90 |
| 0030303S0007 | Mid-Rise\set B | Mid-Site03-Avg | X= 3000 cm, Y= 50 cm, Z= roof height | 0:15:90 |
| 0030303S0008 | Mid-Rise\set B | Mid-Site03-Max | X= 3000 cm, Y= 50 cm, Z= roof height | 0:15:90 |
| 0030303S0009 | Mid-Rise\set B | Mid-Site03-Min | X= 3000 cm, Y= 50 cm, Z= roof height | 0:15:90 |
| 0030303S0010 | Mid-Rise\set B | Mid-Site04-Avg | X= 3000 cm, Y= 50 cm, Z= roof height | 0:15:90 |
| 0030303S0011 | Mid-Rise\set B | Mid-Site04-Max | X= 3000 cm, Y= 50 cm, Z= roof height | 0:15:90 |
| 0030303S0012 | Mid-Rise\set B | Mid-Site04-Min | X= 3000 cm, Y= 50 cm, Z= roof height | 0:15:90 |
| 0030303S0013 | Mid-Rise\set B | Mid-Site05-Avg | X= 3000 cm, Y= 50 cm, Z= roof height | 0:15:90 |
| 0030303S0014 | Mid-Rise\set B | Mid-Site05-Max | X= 3000 cm, Y= 50 cm, Z= roof height | 0:15:90 |

This file is the final accepted version of the manuscript, published in
https://doi.org/10.1061/JSENDH.STENG-12684

| | | | | |
|---|---|---|---|---|
| 0030303S0015 | Mid-Rise\set B | Mid-Site05-Min | X= 3000 cm, Y= 50 cm, Z= roof height | 0:15:90 |
| 0030303S0016 to 0030303S0045 | Mid-Rise\set B | Mid-Site06 to Mid-Site35 | X= 3000 cm, Y= 50 cm, Z= roof height | 0:15:90 |
| 0030303S0046 to 0030303S0056 | Mid-Rise\set C | Mid-Site36 to Mid-Site45 | X= 3000 cm, Y= 50 cm, Z= roof height | 0:15:90 |
| 0030303S0056 to 0030303S0060 | Mid-Rise\set D | Mid-Site46 to Mid-Site50 | X= 3000 cm, Y= 50 cm, Z= roof height | 0:15:90 |

# Figures Caption

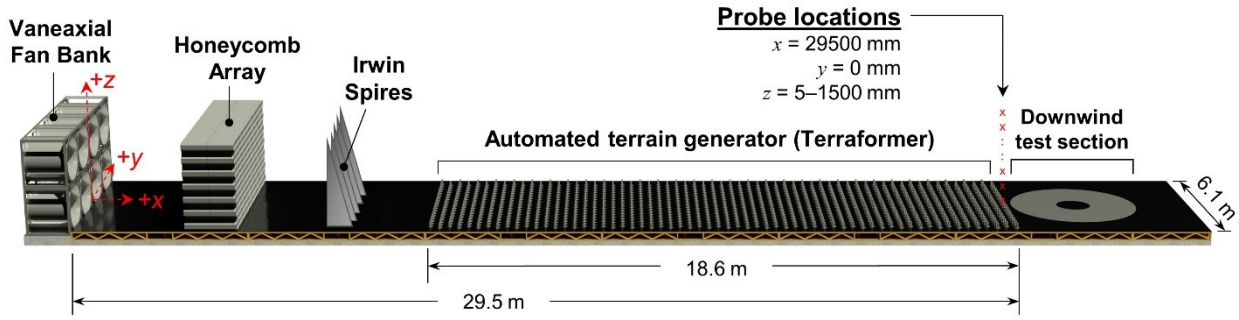


Figure 1: Schematic BLWT profile


Figure 2: The low-rise model with pressure taps installed

This file is the final accepted version of the manuscript, published in
https://doi.org/10.1061/JSENDH.STENG-12684

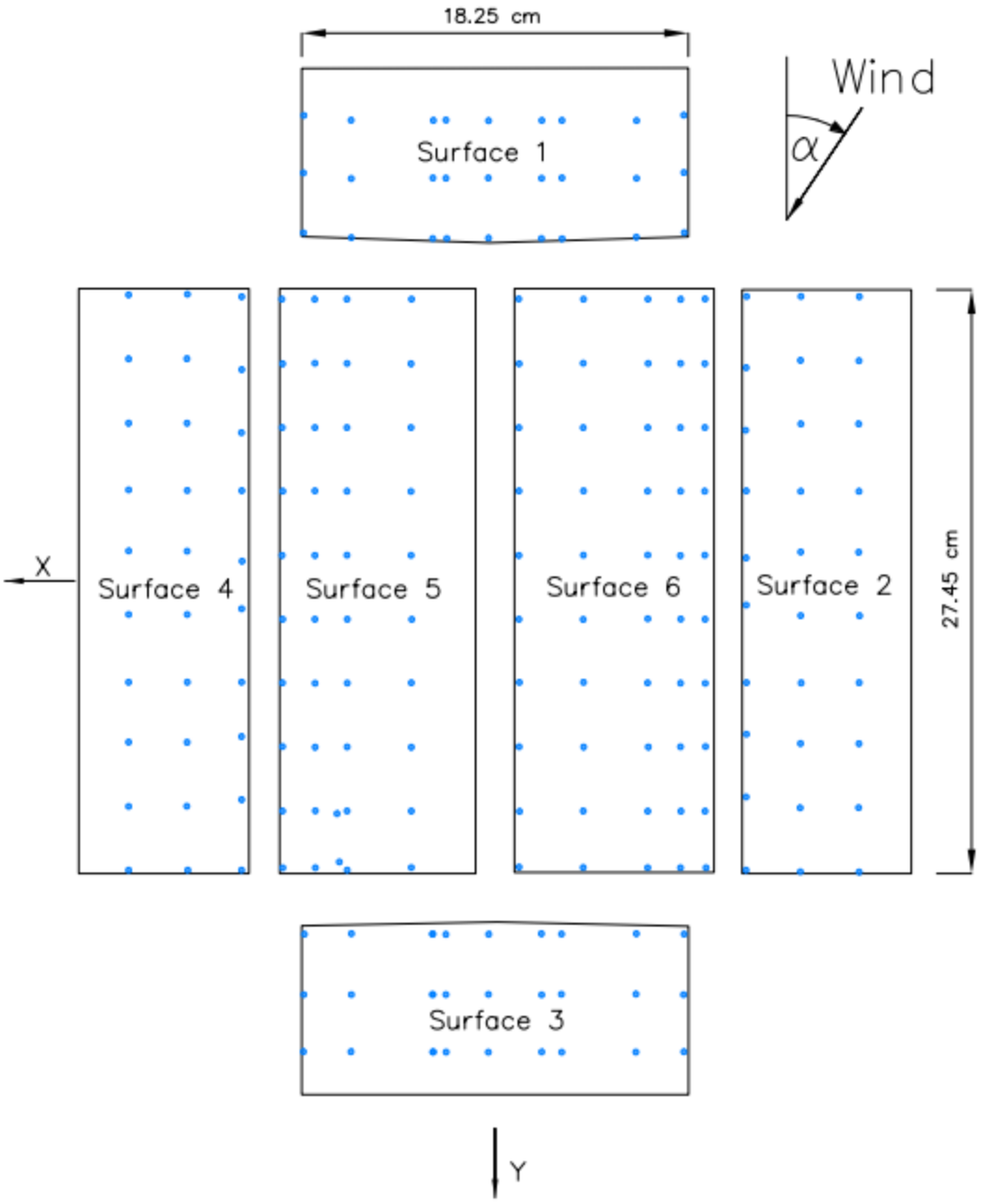


Figure 3: Pressure taps layout of the low-rise model.

This file is the final accepted version of the manuscript, published in
https://doi.org/10.1061/JSENDH.STENG-12684

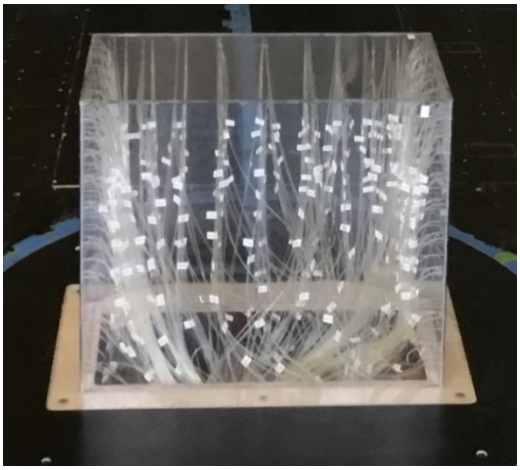

Figure 4: The mid-rise model with pressure taps installed.

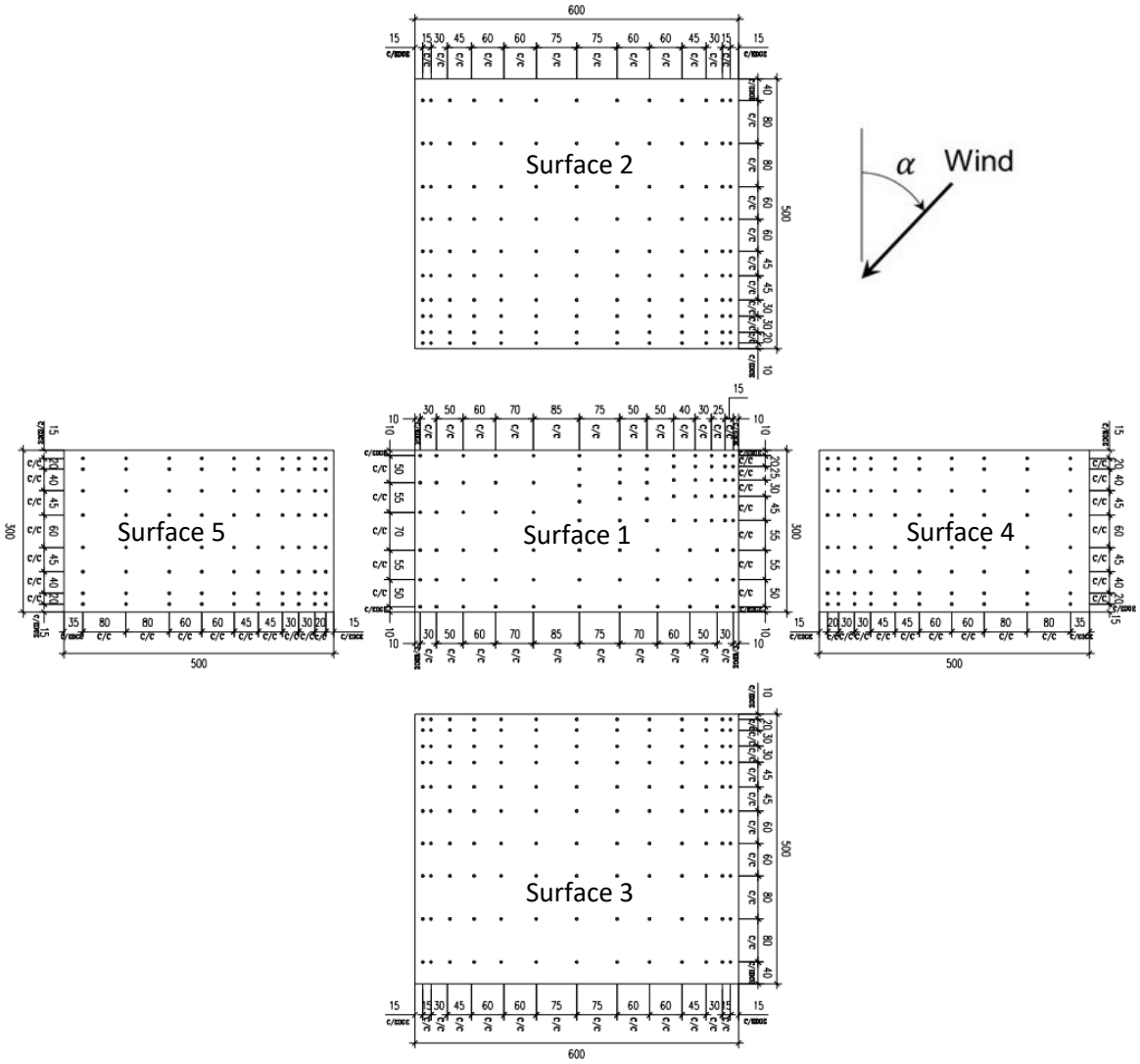

This file is the final accepted version of the manuscript, published in
https://doi.org/10.1061/JSENDH.STENG-12684

Figure 5: Pressure taps layout of the mid-rise model (Units: mm)

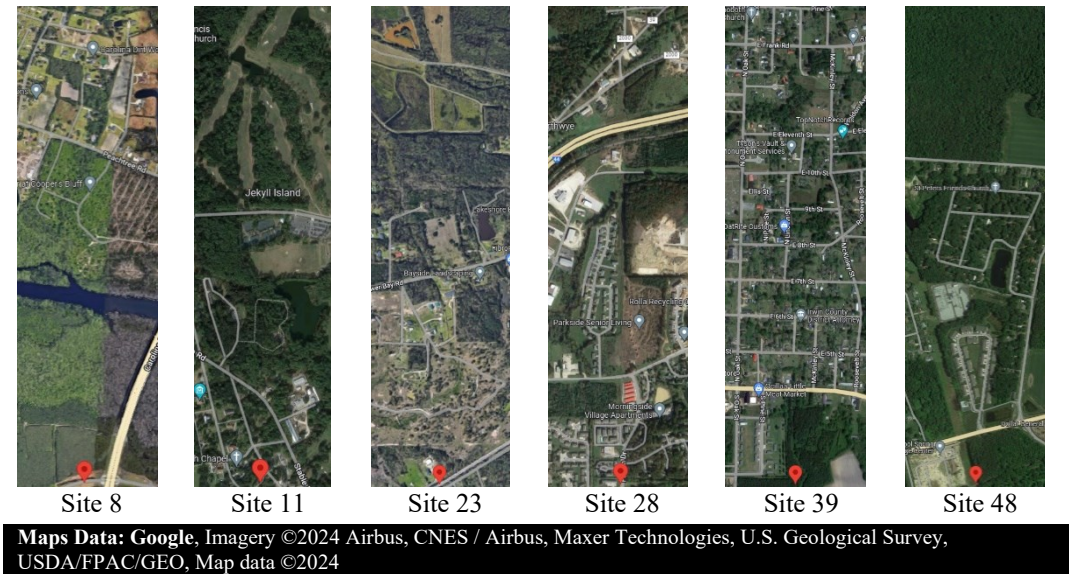


Figure 6: Aerial images of Sites 8, 11, 23, 28, 39, and 48. The location mark at the bottom of the figures shows the measurement location in the wind tunnel and the wind flows from top to bottom. (Map data from Google, Imagery © 2024 Airbus, CNES/ Airbus, Maxer Technologies, U.S. Geological Survey, USDA/FPAC/GEO, Map data ©2024)

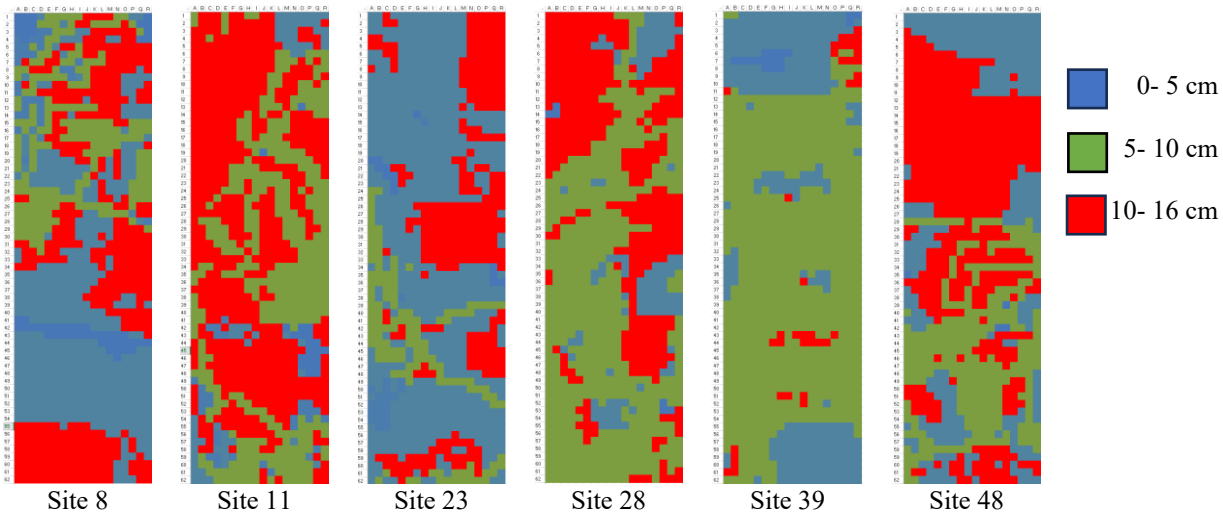


Figure 7: Roughness elements height in the BLWT for Sites 8, 11, 23, 28, 39, and 48.

This file is the final accepted version of the manuscript, published in
https://doi.org/10.1061/JSENDH.STENG-12684

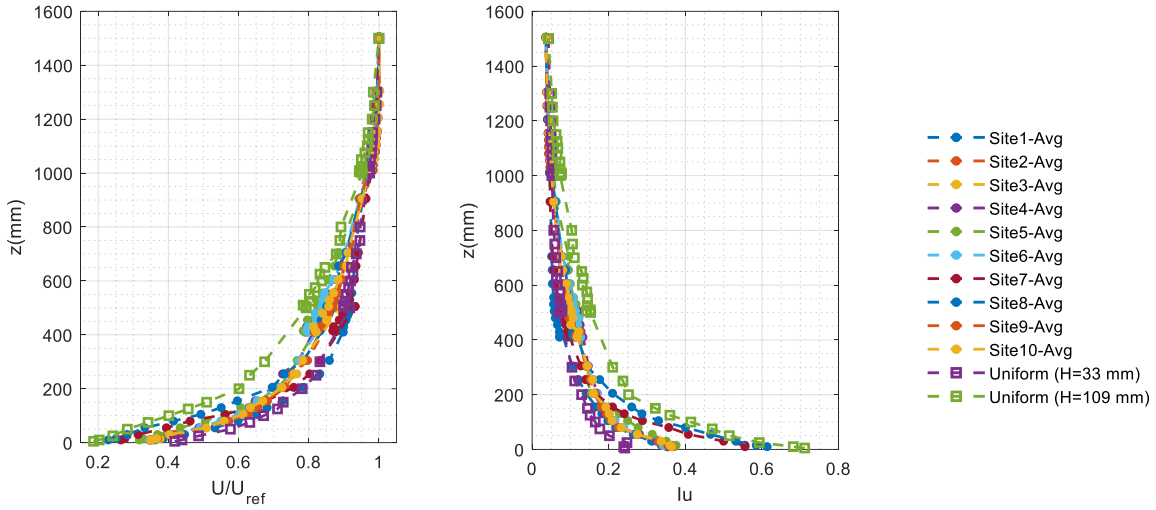


(a) (b)

Figure 8: a) Normalized wind speed profiles of ten nonuniform sites compared with two uniform cases b) Turbulence intensities of ten nonuniform sites compared with two uniform cases. The scale of upwind terrains was 1:100 and the y-axis is in the BLWT scale.

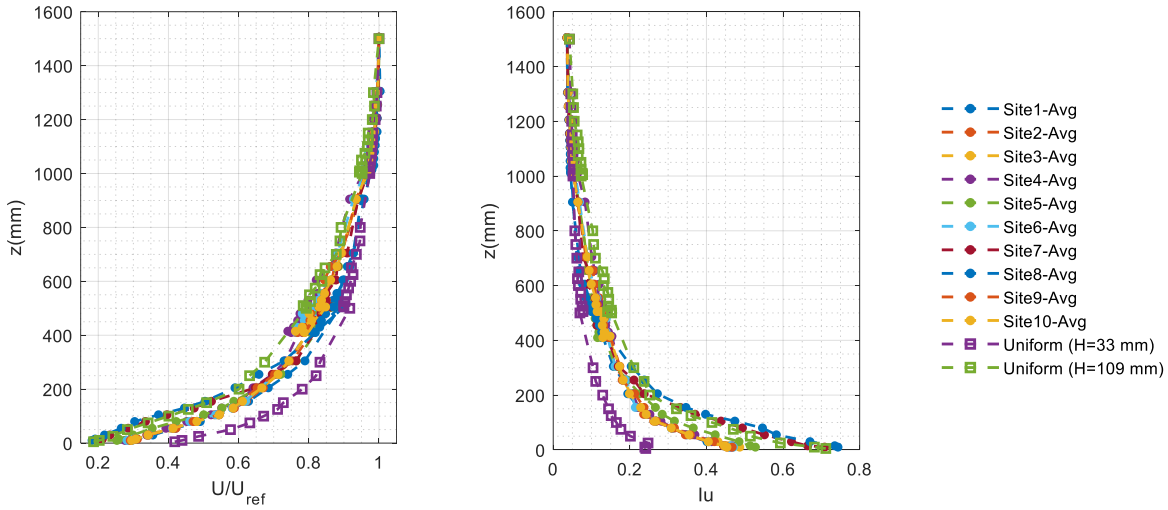


Figure 9: a) Normalized wind speed profiles of ten nonuniform sites compared with two uniform cases b) Turbulence intensities of ten nonuniform sites compared with two uniform cases. The scale of upwind terrains was 1:50 and the y-axis is in the BLWT scale.

This file is the final accepted version of the manuscript, published in
https://doi.org/10.1061/JSENDH.STENG-12684

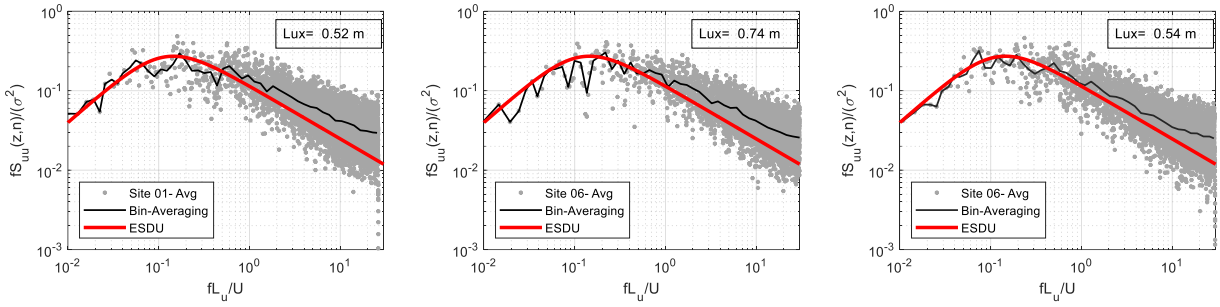


(a) (b) (c)

Figure 10: Wind speed power spectra at 10 m full scale height for a) site 01- Avg case with 1:100 scale, b) site 06- Avg case with 1:100 scale, c) SandyT3-d60- Max case with 1:100 scale

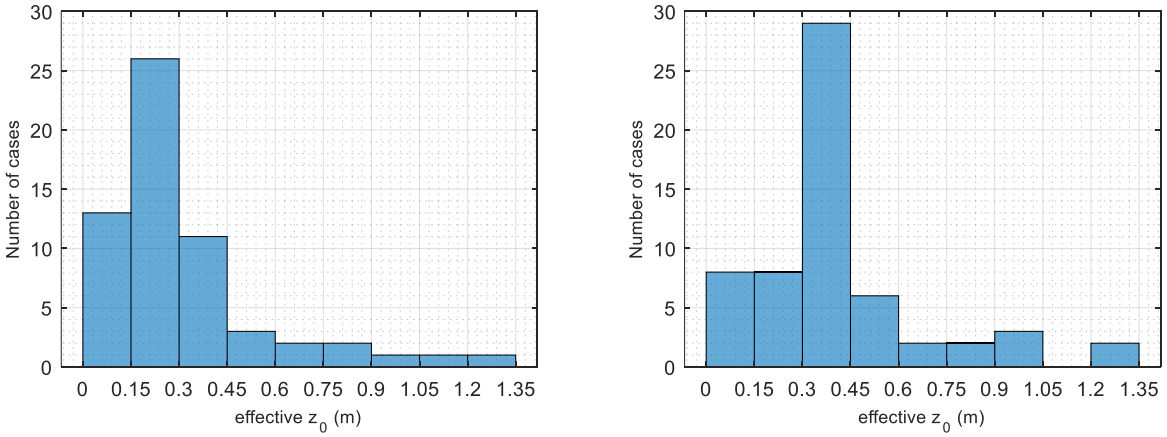


(a) (b)

Figure 11: Effective $z_0$ estimated from wind tunnel measurement for cases in sets B, C and D with a) 1:100 scale and b) 1:50 scale

This file is the final accepted version of the manuscript, published in
https://doi.org/10.1061/JSENDH.STENG-12684

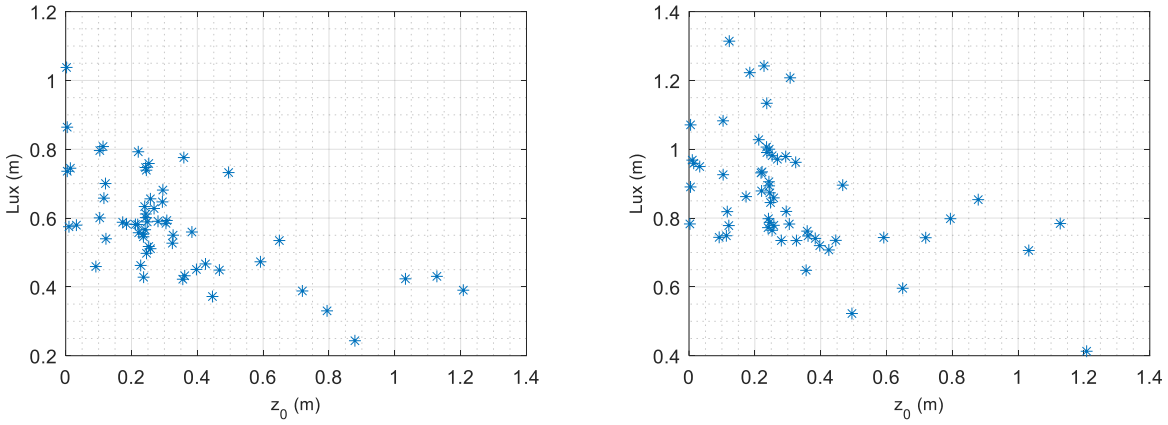


Figure 12: Longitudinal integral length scale at 10 m full scale height vs. effective $z_0$ estimated from wind tunnel measurement for cases in sets B, C and D with a) 1:100 scale and b) 1:50 scale

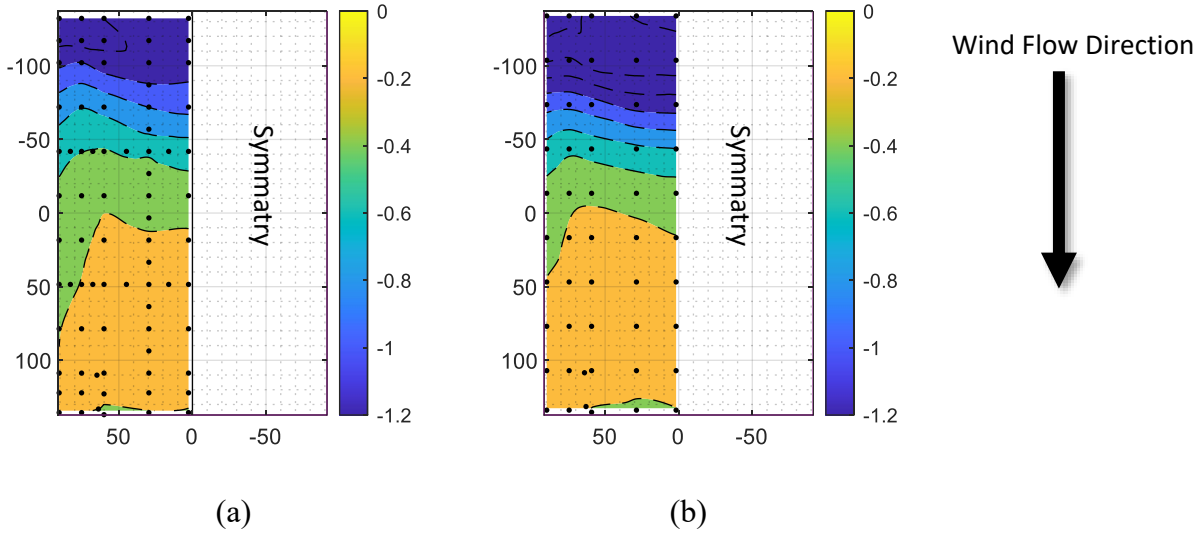


Figure 13: Mean pressure coefficient distribution on the low-rise model roof with 0-degree wind angle of attack for a) uniform case with roughness height of 6 cm and $z_0$ = 0.3 m and b) site03-Avg case (pressure file name = 0030302S0007-000) with $z_0$ = 0.32 m

This file is the final accepted version of the manuscript, published in
https://doi.org/10.1061/JSENDH.STENG-12684

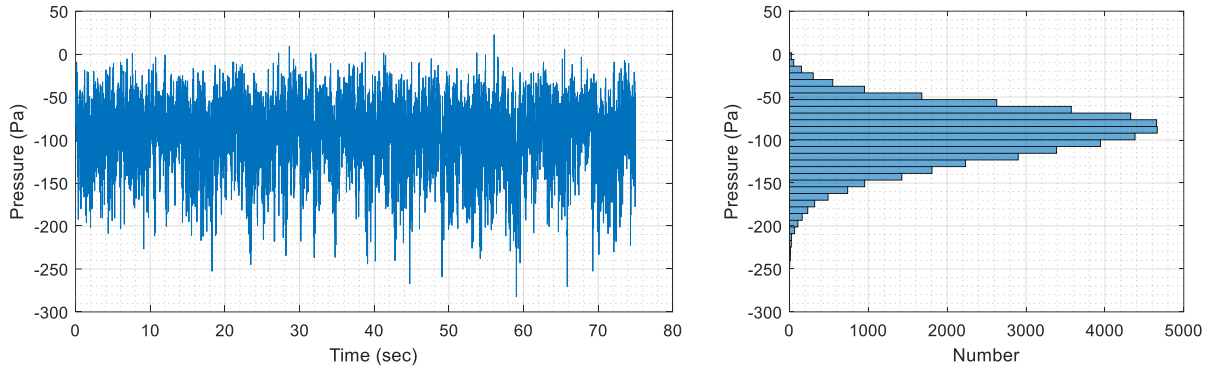


(a) (b)

Figure 14: a) Pressure time series and b) histogram of pressure tap number 401 (see 'Scanivalve.TapData' array in the Matlab files to locate the tap) on low-rise model for site 1- Avg with 15-degree wind angle of attack (pressure file name = 0030302S0001-015)

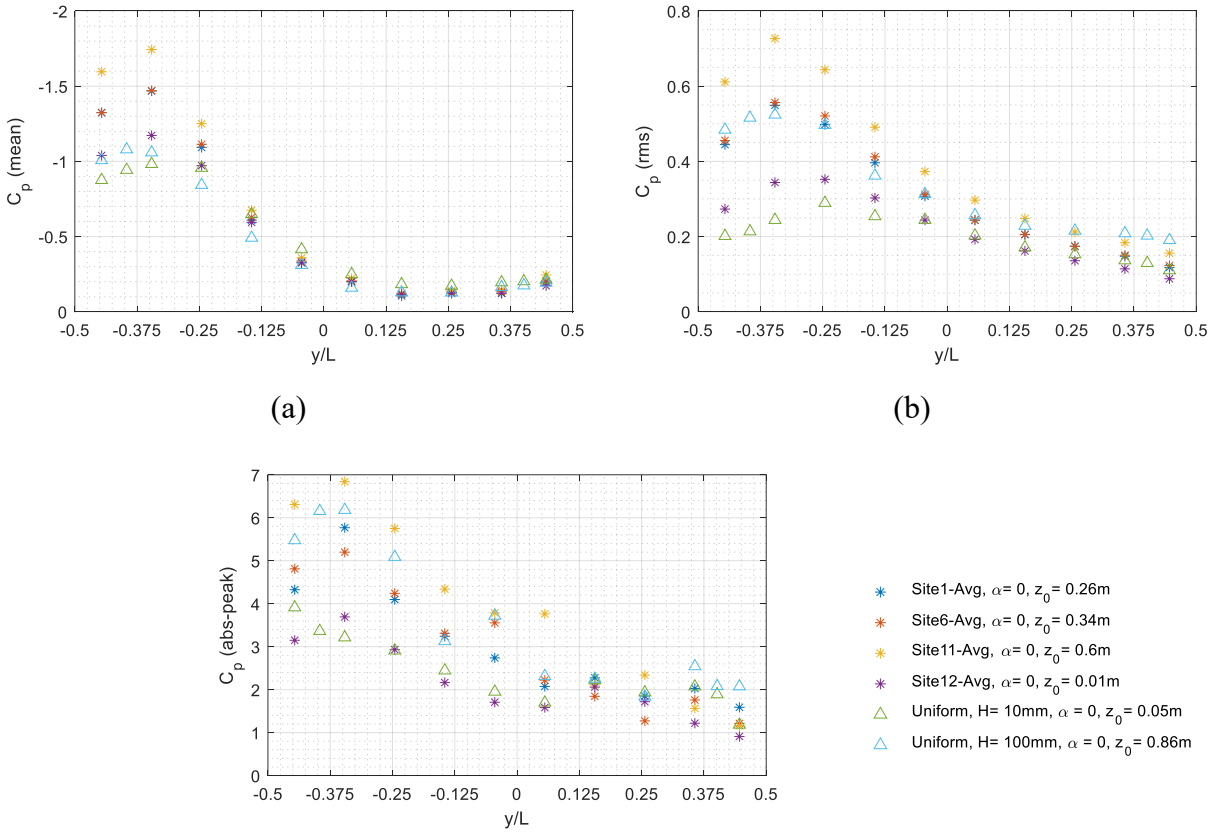


(a) (b)

(c)

Figure 15: Mean, root mean square (rms) and absolute peak (abs-peak) pressure coefficients along the ridge of the low-rise building model for 0-degree wind angle of attack with low-pass filtered data (model scale=1:50)

This file is the final accepted version of the manuscript, published in
https://doi.org/10.1061/JSENDH.STENG-12684

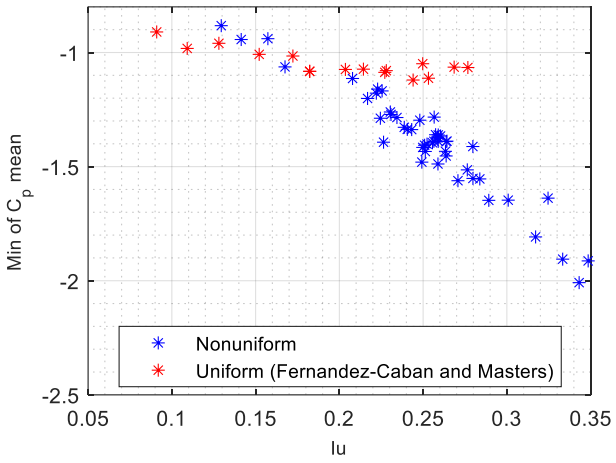


Figure 16: Minimum of mean pressure coefficient along the ridge of the low-rise building model for 0-degree wind angle of attack with low-pass filtered data (model scale=1:50) vs. turbulence intensity at eave height

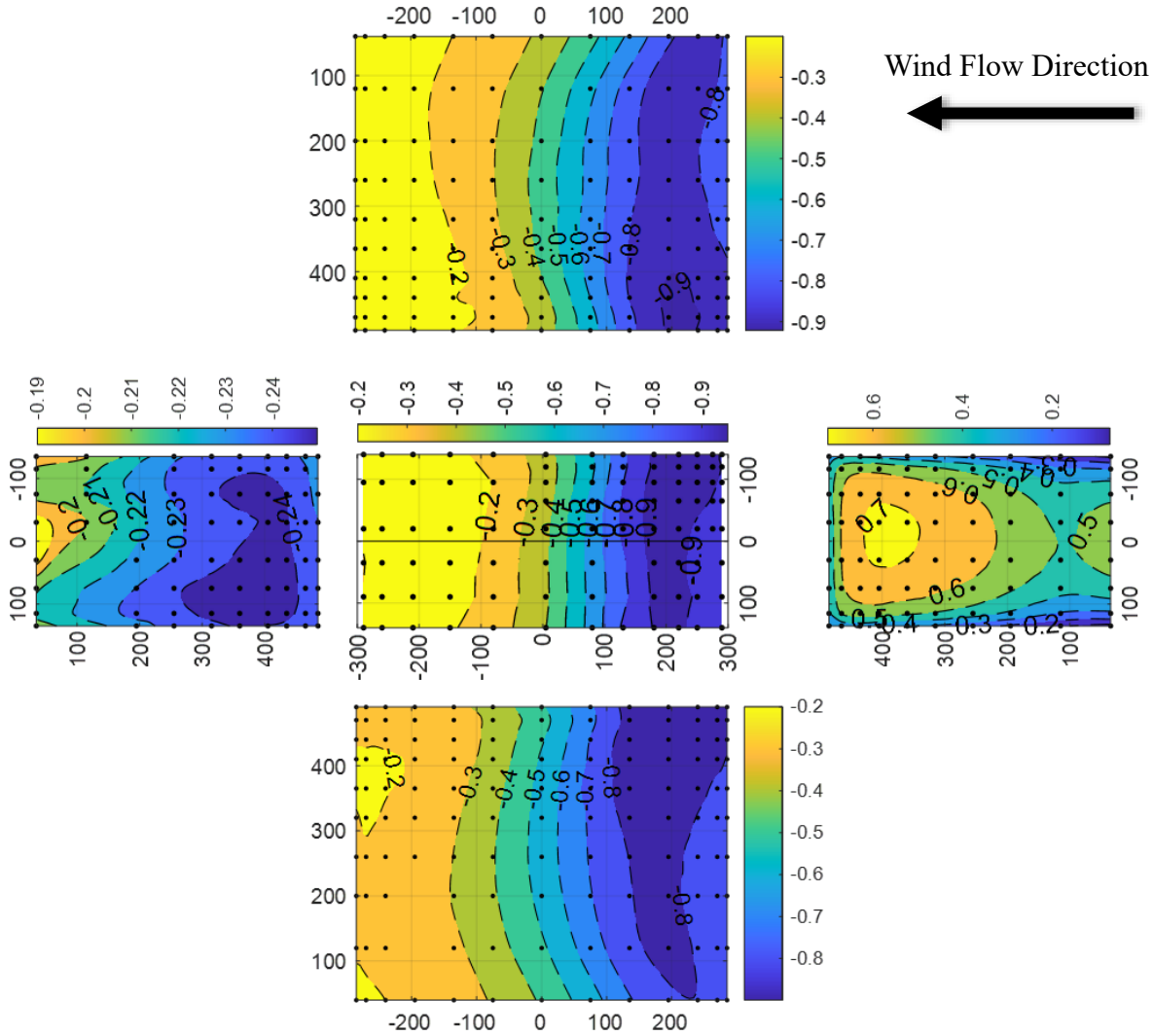

This file is the final accepted version of the manuscript, published in
https://doi.org/10.1061/JSENDH.STENG-12684

Figure 17: Mean pressure coefficient distribution on the mid-rise model with 90-degree angle of attack for site15-Avg case (pressure file name = 0030303S0025-090)

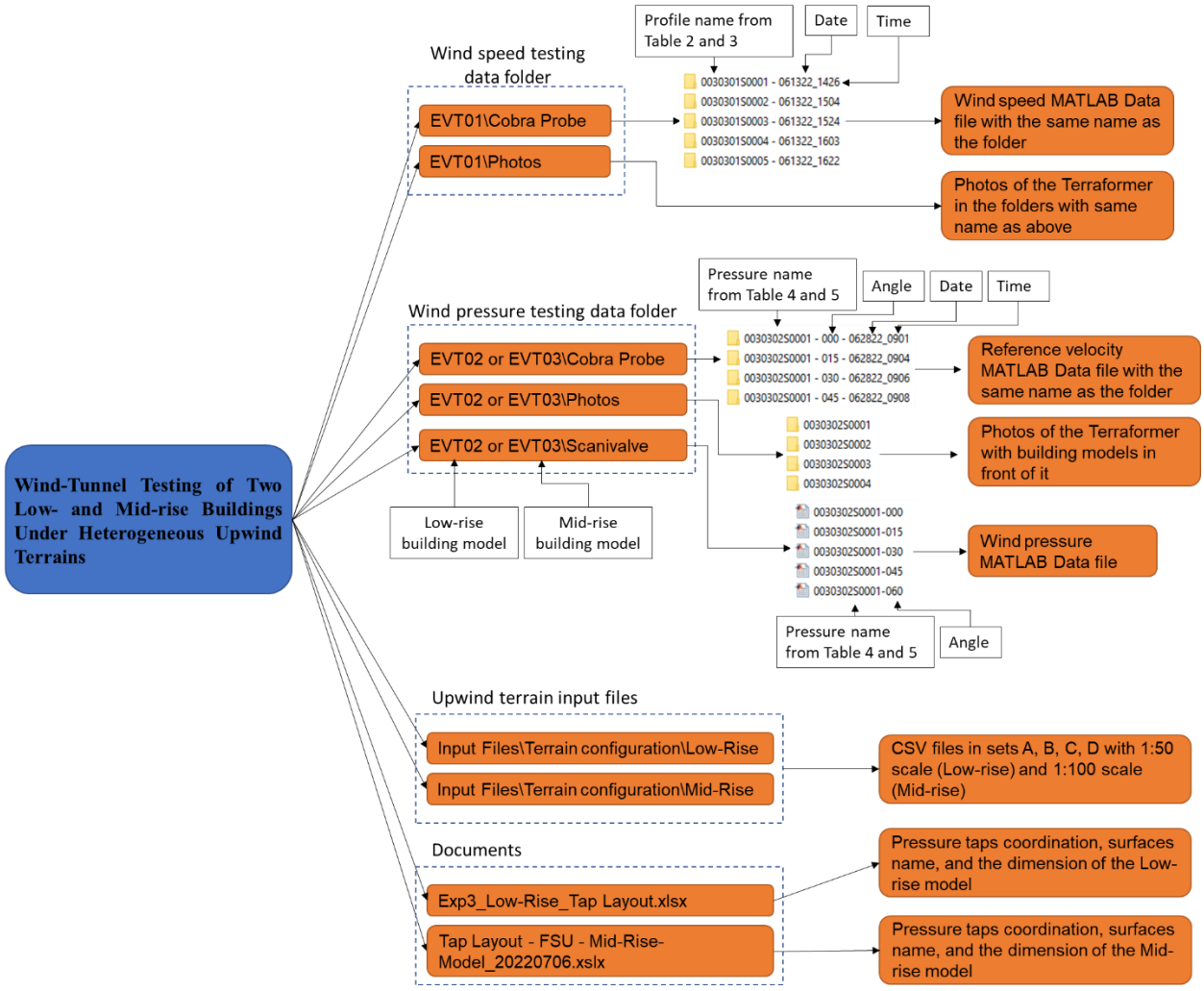


Figure 18: Wind speed and wind pressure data and metadata files organization on the DesignSafe-CI repository